

# A COMPUTATIONAL STUDY OF BULK VISCOSITY EFFECTS ON SHOCK-VORTEX INTERACTION USING DISCONTINUOUS GALERKIN METHOD

S. Singh<sup>1</sup> and R.S. Myong<sup>\*1,2</sup>

<sup>1</sup>Graduate School of Mechanical and Aerospace Engineering, Gyeongsang National Univ.

<sup>2</sup>Dept. of Aerospace and Software Engineering & Research Center for Aircraft Parts Technology, Gyeongsang National Univ.

## 불연속 갤러킨 기법을 이용한 충격파-외류 상호작용에 관한 체적 점성 효과 전산 연구

사티비르 싱,<sup>1</sup> 명 노 신<sup>\*1,2</sup>

<sup>1</sup>경상대학교 대학원 기계항공공학부

<sup>2</sup>경상대학교 항공우주및SW공학전공 및 항공기부품기술연구소

*On the basis of a high order discontinuous Galerkin method, the bulk viscosity effects on shock-vortex interaction are investigated by solving the two-dimensional conservational laws for diatomic gases. A comparison of shock-vortex interaction in monatomic and diatomic gases is conducted. In the case of diatomic gas flow, the substantially strengthened enstrophy evolution is observed. In addition, the effects of interaction parameters such as shock and vortex Mach numbers on shock-vortex interaction are examined. The results show that the strong shock-vortex interaction associated with high shock and vortex Mach numbers can result in higher enstrophy.*

**Key Words :** Bulk viscosity, Diatomic gas, Shock-vortex interaction, Discontinuous Galerkin method

### 1. Introduction

The study of shock-vortex interaction problem has been considered a fundamental issue in aerodynamics and aeroacoustics in the past, due to its wide spectrum of scientific and engineering interests. These include supersonic mixing flows, supersonic jets, its associated ‘shock noise’ and combustion instability[1-3]. In supersonic flows, the interaction between a number of shocks and vortices is significant, and the coupling usually dominates the flow field and makes the flows very complicated.

During the interaction, the shock wave and vortex experience distortion and, as a result, the structure of shock wave and vortex may be altered or destroyed.

In the past, a considerable amount of work has been carried out for better understanding of the sound generation mechanism and the deformation of shock wave and vortex. Ribner developed a linear theory to explain the sound production from the shock-vortex interaction[4]. Inoue and Hattori studied numerically the sound generation mechanism through the interaction of an planar shock wave with a single or a pair of vortices and obtained the first and second acoustic waves of quadrupolar nature[5]. Later, through a numerical simulation with a larger domain, they observed third acoustic wave. Grasso and Pirozzoli studied the shock-vortex interaction problem in wide range of strengths for the shock wave and the vortex, and categorized the interaction into three types,

Received: June 9, 2017, Revised: June 27, 2017,

Accepted: June 27, 2017.

\* Corresponding author, E-mail: myong@gnu.ac.kr

DOI <http://dx.doi.org/10.6112/kscfe.2017.22.2.086>

© KSCFE 2017

depending on the deformation of shock, namely, weak interaction, regular reflection, and Mach reflection[6]. Zhang et al. performed a numerical study of the interaction between a shock wave and a strong vortex and observed multistage features in interaction[7]. Recently, Xiao and Myong studied numerically a microscale shock-vortex interaction problem for argon gas by solving the conservation laws with non-Newtonian coupled constitutive relations[8]. They observed some new interesting features which were not found in macroscale shock-vortex interaction.

Interestingly, virtually all previous studies of shock-vortex interaction are based on compressible Euler or Navier-Stokes theory based on the Stokes' hypothesis. The Stokes's hypothesis has long remained an issue in dispute in gas dynamics in the past[9-12]. It can be easily shown that the Stokes' hypothesis is valid for monatomic gases[10]. The hypothesis is, however, questionable for diatomic gases where the rotational nonequilibrium effect must be taken into account by introducing excess normal stress associated with bulk viscosity[13-15]. For this reason, the bulk viscosity has been the subject of renewed interests, and the current study attempts to make a new contribution to this direction.

In this study, we aim to investigate the bulk viscosity effects of diatomic gas on the shock-vortex interaction. For this purpose, a high order discontinuous Galerkin method is employed to solve the two-dimensional conservation laws numerically. Our study shows that there are considerable differences in flow fields of shock vortex interaction in monatomic and diatomic gases. The effects of bulk viscosity are also investigated in detail for sound pressure, vorticity, and enstrophy which show the complicated physics of the shock-vortex interaction phenomena. In addition, the effects of interaction parameters such as shock and vortex Mach numbers are studied in detail.

### 2. Problem Definition

Fig. 1 presents a schematic diagram of the flow model for the simulation of interaction of a shock wave with a moving vortex. The computational domain is set to be rectangular  $(x_l \leq x \leq x_r, y_b \leq y \leq y_u)$  with  $x_l = -6$ ,  $x_r = 20$ , and  $y_u = -y_b = 15$ . A normal shock wave with the Mach number  $M_s$  is located at  $x = 0$ . Its upstream state is set  $(\rho_0, u_0, v_0, p_0) = (1.0, \sqrt{\gamma} M_s, 0.0, 1.0)$ . The clockwise rotating vortex moves from left to right with

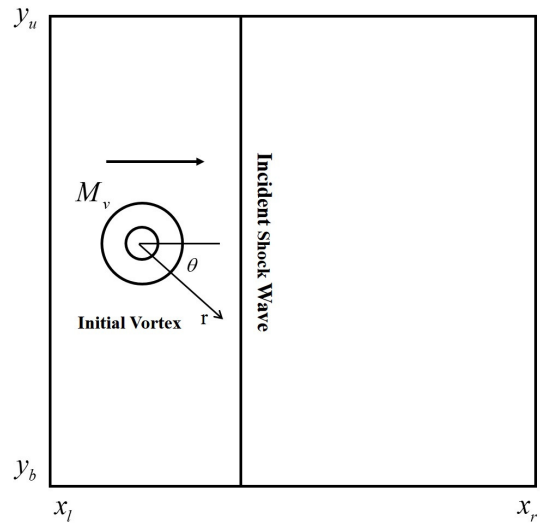


Fig. 1 Schematic diagram of interaction of a shock wave with a moving vortex

respect to the shock wave in the computational domain. The initial position of vortex is considered as  $(x_v, y_v) = (-2, 0)$ .

In the simulation, a composite vortex, consisting an inner core and an outer annular region with uniform velocity at a radius is considered. The tangential velocity distribution of the composite vortex is defined as follows,

$$v_\theta = \begin{cases} u_m \frac{r}{a}, & r \leq a \\ u_m \frac{a}{a^2 - b^2} \left( r - \frac{b^2}{r} \right), & a \leq r \leq b \\ 0, & r \geq b \end{cases} \quad (1)$$

where  $v_\theta$  is the tangential velocity,  $u_m$  is the maximum angular velocity,  $a$  is the inner core radius,  $b$  is the outer annular radius of the composite vortex, and  $r$  is the radius defined as  $r = \sqrt{(x - x_v)^2 + (y - y_v)^2}$ . In present work, the inner core radius  $a = 0.5$  and the outer maximum radius  $b = 1.0$  are used.

The temperature and pressure in the quiescent field surrounding the vortex are prescribed as below. Inside the vortex, pressure, density and energy are determined by balancing the pressure gradients with the centripetal force which is equivalent to solve the following system,

$$\frac{dp}{dr} = \rho \frac{v_\theta^2}{r}, \quad p = \rho RT, \quad \frac{p}{\rho^\gamma} = K, \quad (2)$$

where  $K$  is the constant. From the last two equations, it leads to:

$$\frac{dT}{dr} = \frac{\gamma-1}{R\gamma} \frac{v_\theta^2}{r}. \quad (3)$$

The initial flow field is determined by integrating equations (1), (2) and (3) inside the vortex. For determining the velocity inside the vortex, the radial velocity is added to the free stream velocity.

In the present study, we performed a grid refinement study and found that rectangular  $800 \times 800$  grid points are sufficient for obtaining high resolution solutions. Therefore, all the computational results were carried out on  $800 \times 800$  grid points. Inflow and outflow boundary conditions are introduced at the left and right boundaries, respectively. The upper and lower boundaries are set to be periodic boundary condition. Argon and Nitrogen are considered as monatomic and diatomic gases for simulations.

### 3. Numerical Procedure

#### 3.1. Governing equations for diatomic gases without the Stokes' hypothesis

The Boltzmann-Curtis kinetic equation for diatomic particles with a moment of inertia  $I_m$  and an angular momentum  $\mathbf{j}$  can be expressed as, in case of no external field,

$$\left( \frac{\partial}{\partial t} + \mathbf{v} \cdot \nabla + \frac{\mathbf{j}}{I_m} \cdot \frac{\partial}{\partial \psi} \right) f(\mathbf{v}, \mathbf{r}, \mathbf{j}, \psi, t) = R[f], \quad (4)$$

where  $f$ ,  $\mathbf{v}$ ,  $\mathbf{r}$ ,  $\psi$ ,  $\mathbf{j}$  and  $R[f]$  represent the distribution function, the particle velocity, the particle position, the azimuthal angle associated with the orientation of the particle, the magnitude of the angular momentum vector  $\mathbf{j}$ , the collision integral respectively[14,15]. In gas kinetic theory, there are two different sets of macroscopic variables including the conservative variables  $(\rho, \mathbf{u}, E)$  and the non-conservative variables  $(\Pi, \Delta, \mathbf{Q})$ . These variables can be defined by a statistical formula

$$\Phi^{(k)} = \langle h^{(k)} f \rangle \quad (5)$$

where the angular bracket denotes the integration over the variables  $\mathbf{v}$  and  $\mathbf{j}$ . The  $h^{(k)}$  indicates the molecular expressions for moments. The leading elements of the set

of the conservative variables and non-conservative variables are defined as

$$\begin{aligned} \Phi^{(1)} &= \rho, \quad \Phi^{(2)} = \rho \mathbf{u}, \quad \Phi^{(3)} = \rho E, \quad \Phi^{(4)} = \Pi = [\mathbf{P}]^{(2)}, \\ \Phi^{(5)} &= \Delta = \frac{1}{3} \text{Trace } \mathbf{P} - p, \quad \Phi^{(6)} = \mathbf{Q}, \end{aligned} \quad (6)$$

with the molecular expressions corresponding to this set

$$\begin{aligned} h^{(1)} &= m, \quad h^{(2)} = m \mathbf{v}, \quad h^{(3)} \\ &= \frac{1}{2} m C^2 + H_{rot}, \quad h^{(4)} = [m \mathbf{c} \mathbf{c}]^{(2)}, \\ h^{(5)} &= \frac{1}{3} m C^2 - p/n, \quad h^{(6)} \\ &= \frac{1}{2} m C^2 + H_{rot} - m \hat{h}. \end{aligned} \quad (7)$$

In this expression,  $\rho$  is the density,  $\mathbf{u}$  is the velocity vector,  $E$  is the total energy density,  $p$  is the pressure,  $m$  is the molecular mass,  $\mathbf{c}$  denotes the peculiar velocity of the molecule,  $H_{rot}$  is the rotational Hamiltonian of the particle,  $n$  is the number density of the molecules, and  $\hat{h}$  represents the enthalpy density per unit mass. The symbol  $[ \ ]^{(2)}$  denotes the traceless symmetric part of the second rank tensor.

The  $\Pi, \Delta, \mathbf{Q}$  represent the stress tensor, the excess normal stress, and the heat flux vector, respectively. These stresses are related to the stress tensor  $\mathbf{P}$  through the relation

$$\mathbf{P} = (p + \Delta) \mathbf{I} + \Pi \quad (8)$$

where  $\mathbf{I}$  is unit second rank tensor. The expressions (7) are collision invariants and there is no dissipation term for the conserved variables. Thus the kinetic equation (4) can be derived into a set of evolution equations of conserved variables according to the conservation laws as following,

$$\frac{\partial}{\partial t} \begin{bmatrix} \rho \\ \rho \mathbf{u} \\ \rho E \end{bmatrix} + \nabla \cdot \begin{bmatrix} \rho \mathbf{u} \\ \rho \mathbf{u} \mathbf{u} + p \mathbf{I} \\ (\rho E + p) \mathbf{u} \end{bmatrix} + \nabla \cdot \begin{bmatrix} 0 \\ \Pi + \Delta \mathbf{I} \\ (\Pi + \Delta \mathbf{I}) \mathbf{u} + \mathbf{Q} \end{bmatrix} = 0 \quad (9)$$

The equation (9) can be written in non-dimensional vector form using proper dimensionless variables and parameters as[13],

$$\frac{\partial \mathbf{U}}{\partial t} + \nabla \cdot \mathbf{F}_{inv}(\mathbf{U}) + \nabla \cdot \mathbf{F}_{vis}(\mathbf{U}, \nabla \mathbf{U}) = 0, \quad (10)$$

where the conservative vector  $\mathbf{U}$ , the inviscid flux vector  $\mathbf{F}_{inv}$  and the viscous flux vector  $\mathbf{F}_{vis}$  are given by

$$\mathbf{U} = \begin{bmatrix} \rho \\ \rho \mathbf{u} \\ \rho E \end{bmatrix}, \quad \mathbf{F}_{inv} = \begin{bmatrix} \rho \mathbf{u} \\ \rho \mathbf{u} \mathbf{u} + \frac{1}{\gamma M^2} p \mathbf{I} \\ \left( \rho E + \frac{1}{\gamma M^2} p \right) \mathbf{u} \end{bmatrix}, \quad (11)$$

$$\mathbf{F}_{vis} = \frac{1}{Re} \begin{bmatrix} 0 \\ \mathbf{\Pi} + \Delta \mathbf{I} \\ (\mathbf{\Pi} + \Delta \mathbf{I}) \mathbf{u} + \frac{1}{Ec Pr} \mathbf{Q} \end{bmatrix}.$$

Here the dimensionless numbers, Mach( $M$ ), Reynolds( $Re$ ), Eckert( $Ec$ ) and Prandtl( $Pr$ ), can be defined as

$$M \equiv \frac{u_r}{\sqrt{\gamma R T}}, \quad Re \equiv \frac{\rho_r u_r L}{\mu_r}, \quad (12)$$

$$Ec \equiv (\gamma - 1) M^2, \quad Pr \equiv \frac{C_{p,r} \mu_r}{k_r},$$

where the subscript  $r$  stands for the reference state,  $\gamma$  is the specific heat ratio,  $T$  is the temperature,  $R$  is the gas constant, and  $C_{p,r}$  is the reference heat capacity per mass at constant pressure.

For the classical Navier-Fourier model, the stress tensor  $\mathbf{\Pi}$ , the excess normal stress  $\Delta$ , and the heat flux vector  $\mathbf{Q}$  are computed by the Newtonian law of shear and bulk viscosity and the Fourier law of heat conduction, respectively, as follows,

$$\mathbf{\Pi} = -2\mu [\nabla \mathbf{u}]^{(2)}, \quad \Delta = -\mu_b \nabla \cdot \mathbf{u}, \quad \mathbf{Q} = -k \nabla T, \quad (13)$$

where  $\mu$ ,  $\mu_b$  and  $k$  are the Chapman-Enskog viscosity, bulk viscosity, and the thermal conductivity, respectively, for the diatomic molecules and can be expressed as,

$$\mu = T^s, \quad \mu_b = f_b \mu, \quad k = T^s, \quad \text{and } s = \frac{1}{2} + 2/(\nu - 1), \quad (14)$$

where  $f_b$  is the ratio of the bulk viscosity and shear viscosity which can be calculated by the sound wave absorption measurement. The  $f_b$  value for argon and nitrogen gases are prescribed as 0.0 and 0.8, respectively [15]. The  $\nu$  denotes the exponent of the inverse power laws for the gas particle interaction potentials.

### 3.2. Discontinuous Galerkin formulation

The spatial discretization of the Navier-Fourier equations

is based on a mixed DG formulation proposed by Bassi and Rebay[16]. This formulation determines the value of the second-order derivatives present in viscous terms by adding auxiliary unknowns  $\mathbf{S}$ , because the second-order derivatives cannot be accommodated directly in a weak formulation using a discontinuous function space. Therefore,  $\mathbf{S}$  can be defined as the derivative of either primitive or conservative variables  $\mathbf{U}$ . Hence, equation (10) can be reformulated as the coupled system for  $\mathbf{S}$  and  $\mathbf{U}$  as

$$\frac{\partial \mathbf{U}}{\partial t} + \nabla \cdot \mathbf{F}_{inv}(\mathbf{U}) + \nabla \cdot \mathbf{F}_{vis}(\mathbf{U}, \mathbf{S}) = 0, \quad (15)$$

$$\mathbf{S} - \nabla \mathbf{U} = 0.$$

In order to discretize the coupled system (15), the computational domain is decomposed into uniform square elements. The exact solutions of  $\mathbf{U}$  and  $\mathbf{S}$  are approximated by the DG polynomial approximations of  $\mathbf{U}_h$  and  $\mathbf{S}_h$ , respectively,

$$\mathbf{U}_h = \sum_{i=0}^{N_k} u_h^i(t) \phi^i(\mathbf{x}), \quad (16)$$

$$\mathbf{S}_h = \sum_{i=0}^{N_k} s_h^i(t) \phi^i(\mathbf{x}), \quad \forall \mathbf{x} \in \Omega_e,$$

where  $u_h^i(t)$  and  $s_h^i(t)$  are the local degrees of freedom of  $\mathbf{U}$  and  $\mathbf{S}$ , the  $\phi^i(\mathbf{x})$  is the basis functions for finite element space, while  $N_k$  is the number of required basis function for the  $k$ -exact DG approximation. In this work, the second order of scaled Legendre basis functions and the third order DG scheme are adopted for square elements. The mixed system (15) is multiplied with the test function, which is taken to be equal to the basis function  $\phi^i(\mathbf{x})$ , and then integrated by parts over an element  $\Omega_e$ . It results in the weak formulation of the mixed system for  $\mathbf{U}_h$  and  $\mathbf{S}_h$ ,

$$\begin{aligned} & \frac{\partial}{\partial t} \int_{\Omega_e} \mathbf{U}_h \phi dV - \int_{\Omega_e} \nabla \phi \cdot \mathbf{F}_{inv} dV - \int_{\Omega_e} \nabla \phi \cdot \mathbf{F}_{vis} dV \\ & + \int_{\partial \Omega_e} \phi \mathbf{F}_{inv} \cdot \mathbf{n} d\Gamma + \int_{\partial \Omega_e} \phi \mathbf{F}_{vis} \cdot \mathbf{n} d\Gamma = 0, \\ & \int_{\Omega_e} \mathbf{S}_h \phi dV + \int_{\Omega_e} \nabla \phi \mathbf{U}_h dV - \int_{\partial \Omega_e} \phi \mathbf{U}_h \cdot \mathbf{n} d\Gamma = 0, \end{aligned} \quad (17)$$

where  $\mathbf{n}$  is the outward normal vector,  $V$  and  $\Gamma$  denote

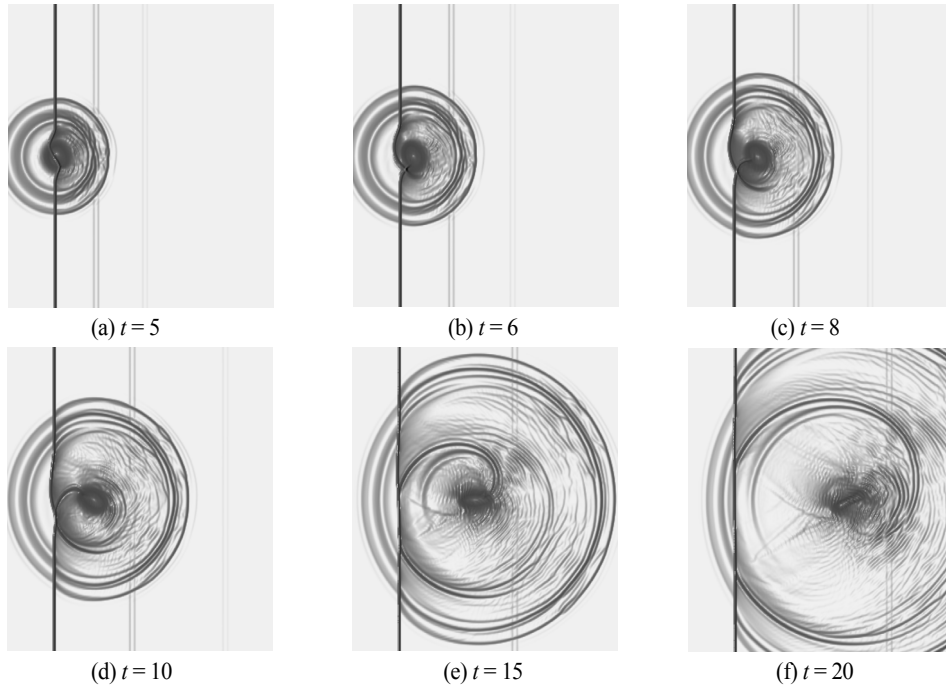


Fig. 2 The time evolution of flow structure: cell-averaged numerical shadowgraph obtained from  $\nabla^2 \rho$  at  $M_s = 1.2$ ,  $M_v = 0.5$ ,  $f_b = 0.8$

the volume and boundary of the element, respectively. In the present study, the Gaussian-Legendre quadrature rule has been implemented for both boundary and volume integrations. Therefore, the volume and boundary integrals in equation (17) are computed using  $2k$  and  $2k+1$  order accurate Gauss quadrature formulas, respectively[17]. Three quadrature points on edges and nine quadrature points inside the elements are used for boundary and volume integrations. In present work, the numerical fluxes, local Lax-Friedrichs and BR1 scheme are used for inviscid and viscous terms, respectively[17]. The nonlinear total variation bounded(TVB) limiter proposed by Shu[18] is used for controlling the spurious oscillation in the solutions. The third order total variation diminishing Range-Kutta(TVD-RK) method is employed for time integration.

The present numerical method and the code have been validated in our previous work[8]. The interaction parameters are  $M_s$  and  $M_v$ , where  $M_s$  denotes the speed of incident shock wave, while  $M_v$  measures the strength of the vortex. The shock Mach number is adopted to be  $M_s = 1.05, 1.2$  and  $1.5$ . The vortex Mach number  $M_v$  ranges from  $0.5$  to  $1.0$ .

## 4. Results and Discussion

In this section, we present the numerical results for shock-vortex interaction of diatomic gas.

### 4.1. Time evolution of flow structure

Fig. 2 illustrates the six snapshots of time evolution of the flow structure for shock-vortex interaction with  $M_s = 1.2$ ,  $M_v = 0.5$ ,  $f_b = 0.8$ . These snapshots are cell-averaged shadow graphs that are sensitive to the density gradient and can provide the main features of flow structure. When the outer flow field of the vortex interacts with the incident shock wave, the upper and lower portions of the shock wave are diffracted around the vortex. As a result, the shock wave is distorted into an S shape by vortex as seen in Fig. 2(a). An expansion by the leading shock and a compression by the lagging shock are generated during interaction, leading to a quadrupolar structure in the vortex. In Fig. 2(b), the leading shock breaks out from the vortex and becomes an accelerated shock in contrast to the lagging shock held by the vortex. After breaking out from shock wave, the vortex begins to

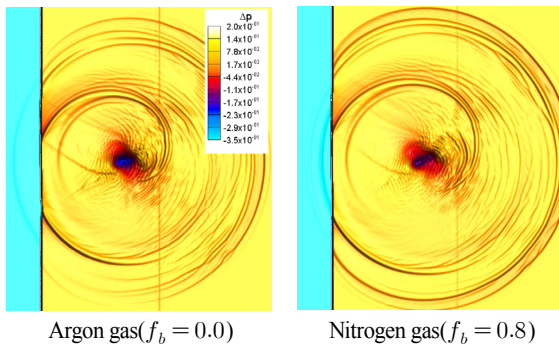


Fig. 3 Bulk viscosity effect: cell-averaged sound pressure contours at  $M_s = 1.2, M_v = 0.5$

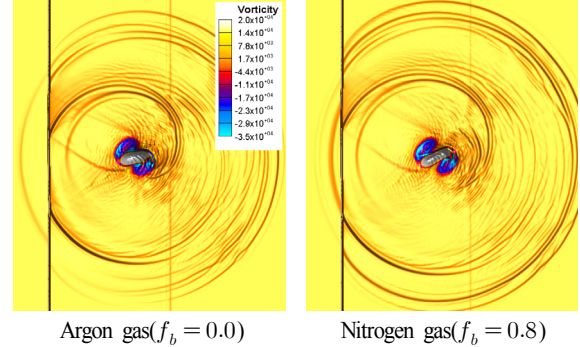


Fig. 4 Bulk viscosity effect: cell-averaged vorticity contours at  $M_s = 1.2, M_v = 0.5$

revolve. In Fig. 2(c), the accelerated shock wave and the captured shock wave produce a regular reflection type(RR type) configuration. In Fig. 2(d)-(f), the shock-shock interaction becomes stronger and produces a Mach reflection type(MR type) configuration. In addition, two slip lines are merged into one and dragged into the vortex core in a spiral from by the revolving vortex.

**4.2. Bulk viscosity effects: sound pressure, vorticity, and enstrophy**

For demonstrating the effects of bulk viscosity of diatomic gases on shock-vortex interaction, two test cases are considered: one for monatomic gas(argon,  $f_b = 0.0$ ) and another for diatomic gas(nitrogen,  $f_b = 0.8$ ) with  $M_s = 1.2, M_v = 0.5$ .

Fig. 3 displays the sound pressure contours for shock-vortex interaction for argon and nitrogen gases at  $t = 20$ . The sound pressure is defined as

$$\Delta p = \frac{p - p_s}{p_s}, \tag{18}$$

where  $p_s$  is the pressure behind the shock wave.

In the figure, the positive  $\Delta p$  region represents the compression region and the negative  $\Delta p$  region denotes the rarefaction region. The results shows that a large rarefaction region is observed near the vortex core for argon gas, whereas the rarefaction region is found in a small scale in case of nitrogen case. In addition, the results show that the expansion of reflected shock waves for nitrogen gas is found larger and stronger in contrast with argon gas after the interaction with vortex. In both gases, the reflected shock waves exhibit a quadrupolar

nature.

In shock-vortex interaction problem, the vorticity plays a important role for describing the physics of interaction. It can be defined as,

$$\Omega_z = \frac{\partial v}{\partial x} - \frac{\partial u}{\partial y}. \tag{19}$$

Fig. 4 shows the distribution of vorticity in shock-vortex interaction for argon and nitrogen gases at  $t = 20$ . The numerical results show that both gases have different vorticity distribution pattern. In our simulations, we used a composite vortex which shows a positive vorticity inside the core and negative vorticity outside of the angular ring. The numerical results show a decrease in positive vorticity and increase in negative vorticity due to viscous effects. For argon gas, the inner core of vortex composed of positive vorticity is stretched in horizontal elliptical form, and the outer negative region is detached with the inner core. On the other hand, this stretching is more pronounced for nitrogen gas.

The mechanisms leading to the generation or attenuation of vorticity in the interaction can be investigated by studying the time evolution of the enstrophy which can be expressed as

$$Enstrophy(t) = \int_{\partial A} \Omega_z^2(x,y,t) dx dy, \tag{20}$$

where  $\partial A$  is the area of the computational domain.

Fig. 5 illustrates the time evolution of enstrophy in shock-vortex interaction for argon and nitrogen gas flows. It is observed that both gases have almost similar enstrophy patterns as it increase significantly up to 700 ns

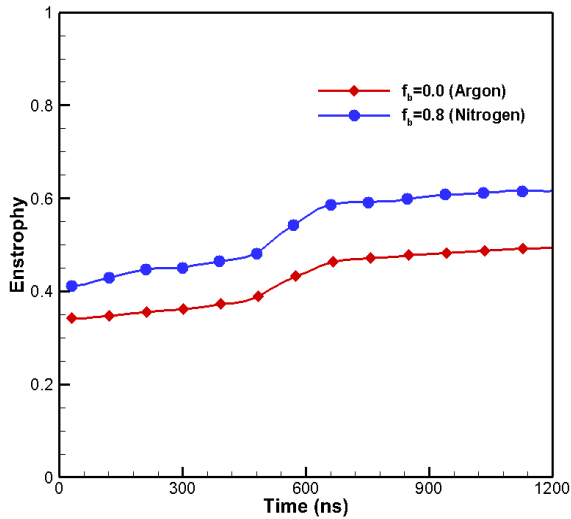


Fig. 5 Bulk viscosity effect: time evolution of enstrophy at  $M_s = 1.2, M_v = 0.5$

and, after that, it becomes almost constant. But the values of enstrophy increase are found different for both gases. The increase in argon gas is found 0.5, while the value show a large jump up to 0.6 in case of nitrogen gas. It may be concluded that difference in enstrophy is caused by the bulk viscosity effect.

4.3. Effect of interaction parameter: shock Mach number

Three cases are selected to explain the effect of the shock Mach numbers:  $M_s = 1.05, 1.2, 1.5$  with same shock Mach number  $M_v = 1.2$  and  $f_b = 0.8$ . The sound pressure and the vorticity contours for different incident shock Mach numbers at  $t = 20$  are illustrated in Fig. 6. The results show that, as expected, low Mach number causes weaker shock-vortex interaction and the vortex experiences less distortion as shown in Fig. 6(a). As the shock Mach number increases, the interaction between shock and vortex becomes stronger and the vortex is more distorted that can be seen in Fig. 6(b) and 6(c). In

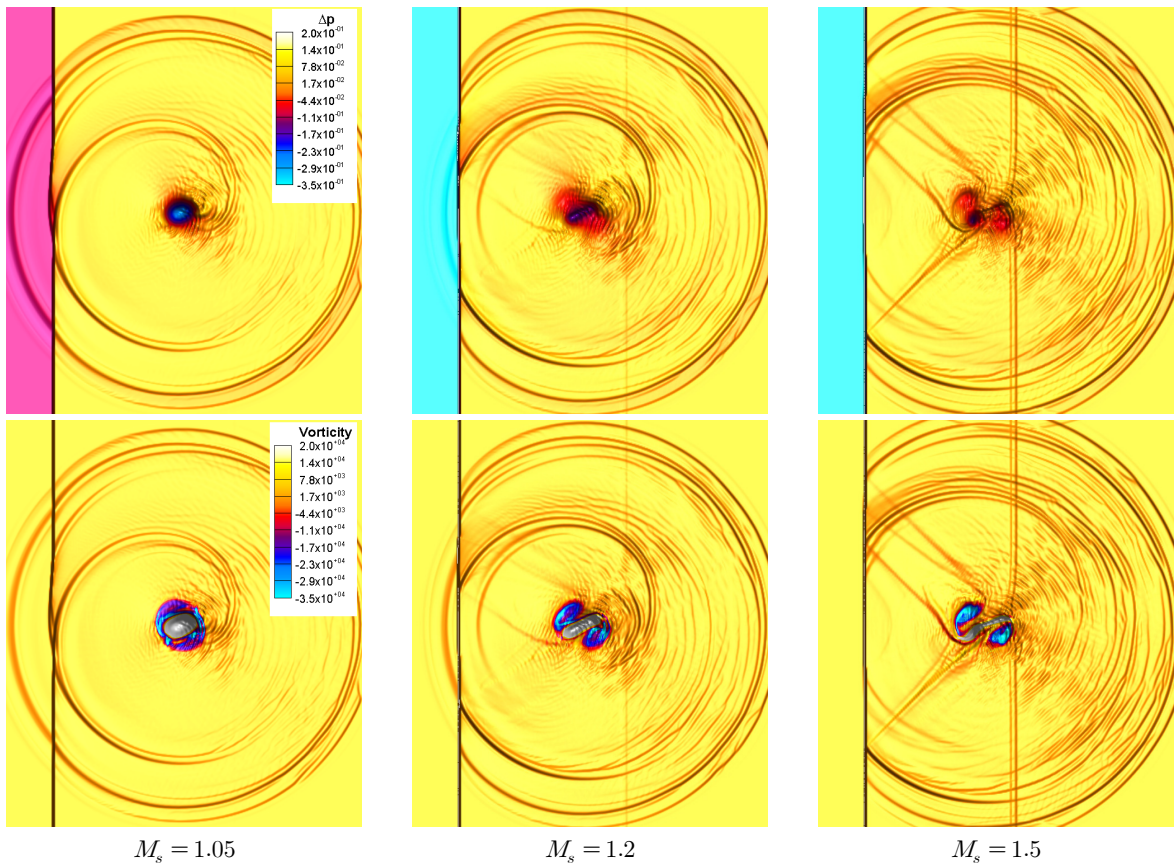


Fig. 6 Shock Mach number effect: cell-averaged sound pressure (top) and vorticity (bottom) contours at  $M_v = 0.5, f_b = 0.8$

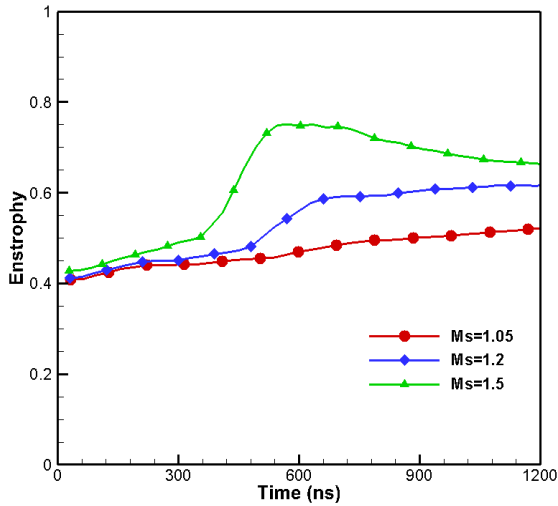


Fig. 7 Shock Mach number effect: time evolution of enstrophy at  $M_v = 0.5, f_b = 0.8$

addition, the shock wave with high Mach number blocks the diffusion of the expansion waves caused by the vortex. Generally, the high shock Mach number cases diminish the vortex region and increase the compression and rarefaction regions.

The effect of shock Mach number can further be examined through the distribution of vorticity. Three different patterns of vorticity distribution are observed for three different  $M_s$  values after interaction, as seen in Fig. 6. It may be noted that the vortex is deformed after interaction, as depicted from the vorticity distribution. At  $M_s = 1.05$ , the interaction between shock and vortex is weak, which results in circular shape in the vorticity distribution, as seen in Fig. 6(a). As the shock Mach number increases, the shape of vorticity distribution becomes non-circular. At  $M_s = 1.2, 1.5$ , it appears highly squeezed in the longitudinal direction, as seen in Fig. 6(b) and 6(c).

The effects of shock Mach number can be investigated

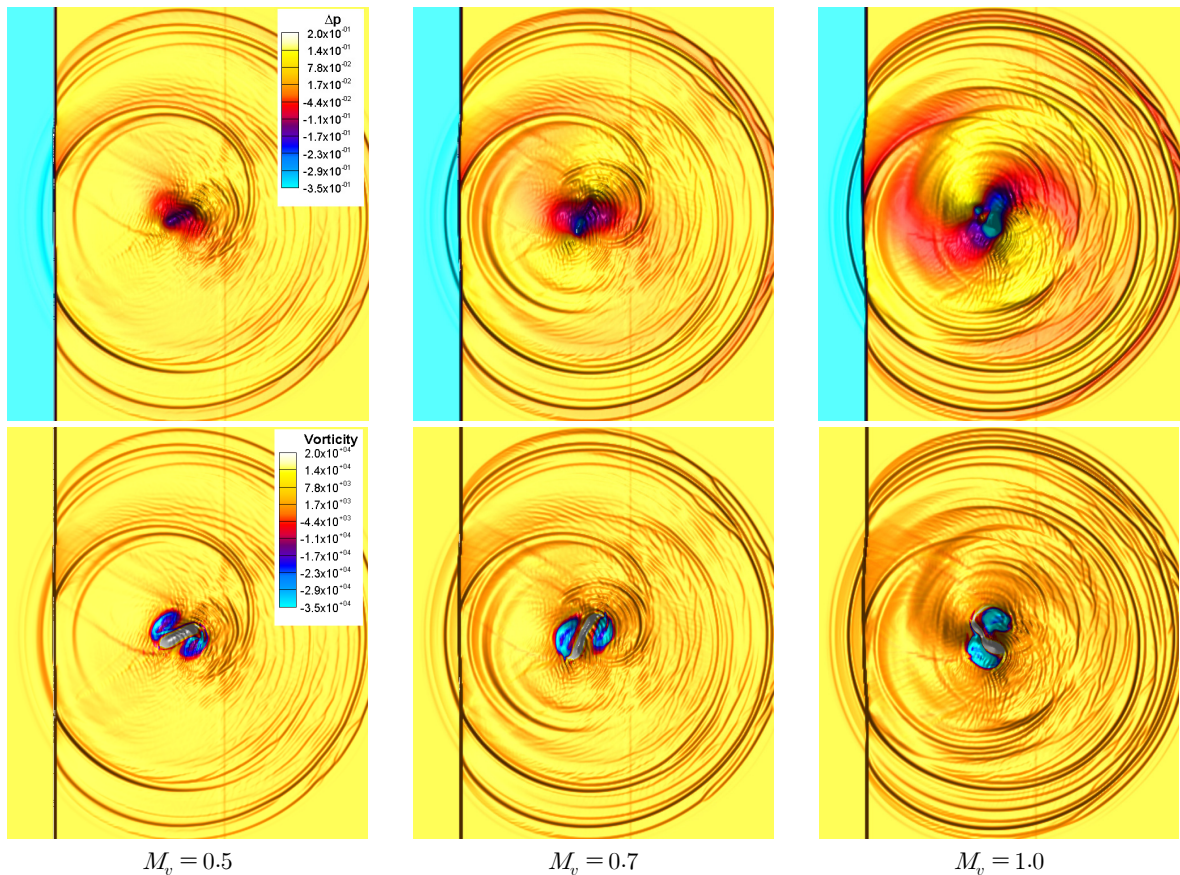


Fig. 8 Vortex Mach number effect: cell-averaged sound pressure (top) and vorticity (bottom) contours at  $M_s = 1.2, f_b = 0.8$

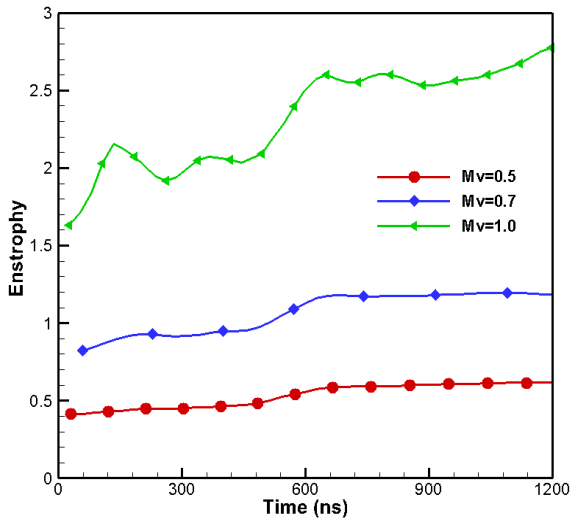


Fig. 9 Shock Mach number effect: time evolution of enstrophy at  $M_s = 1.2$ ,  $f_b = 0.8$

based on the time evolution of enstrophy, as plotted in Fig. 7. The result shows that the shock wave begins to interact with vortex around 400 ns and ends around 800 ns. The trend of enstrophy at  $M_s = 1.05$  is quite different from the other cases  $M_s = 1.2$  and  $M_s = 1.5$ . During interaction, a small increase in enstrophy is observed for  $M_s = 1.05$ , while a large increase is observed at  $M_s = 1.2$  and  $M_s = 1.5$ .

#### 4.4. Effect of interaction parameter: vortex Mach number

Three cases are selected to investigate the effect of the vortex Mach numbers:  $M_v = 0.5, 0.7, 1.0$  with the same shock Mach number  $M_s = 1.2$  and  $f_b = 0.8$ . Fig. 8 shows the sound pressure and vorticity contours after interaction at  $t = 20$ . The numerical results show that, as expected, the decreasing vortex Mach number weakens the shock-vortex interaction and causes a reduction in compression regions. As the vortex Mach number increases, the shock interaction becomes stronger, resulting in enlargement in compression and rarefaction regions.

The distribution of vorticity may be also useful for analysing the effect of vortex Mach number. It is observed in Fig. 8 that, as the vortex Mach number increases, the negative vorticity increases, and the positive vorticity detached with negative vorticity shows pronounced change.

Fig. 9 illustrates the time evolution of enstrophy that is useful in explaining the effect of vortex Mach number. The results show that the enstrophy increment increases

with increasing the vortex Mach number. During the interaction, considerable enstrophy increase is observed at high vortex Mach number, whereas a very small enstrophy increment is found at low vortex Mach number.

## 5. Conclusion

In this study, the interaction of shock wave with moving a vortex is simulated by solving two-dimensional conservation laws for diatomic gases in order to investigate the bulk viscosity effect. A discontinuous Galerkin method of high order spatial accuracy is employed to solve the conservation laws.

The time evolution of flow structure of shock-vortex interaction for diatomic gas is discussed in detail. The results show that the reflected shock waves of quadrupolar nature can produce Mach reflection configuration after interaction. A detailed comparison of shock-vortex interaction simulations between monatomic and diatomic gases is also conducted to examine the bulk viscosity effect. The numerical results show a considerable discrepancy for different bulk viscosity values. Moreover, the effects of interaction parameters such as shock and vortex Mach numbers on the shock-vortex interaction are investigated. It is found that strong interactions occur whenever a strong shock interacts with a strong vortex, which results in a noticeable increase in the enstrophy.

## Acknowledgements

This work was supported by the National Research Foundation of Korea funded by the Ministry of Education, Science and Technology (NRF 2015-M1A3A3A02010621 and 2017-R1A2B2007634), South Korea.

## References

- [1] 1983, Pao, S.P. and Seiner, J.M., "Shock-associated noise in supersonic jets," *AIAA Journal*, Vol.21, pp.687-693.
- [2] 1991, Lu, P.J. and Wu, K.C., "On the shock enhancement of confined supersonic mixing flows," *Physics of Fluids A*, Vol.2, pp.3046-3062.
- [3] 1998, Smart, M.K., Kalkhoran, I.M. and Popovic, S., "Some aspects of streamwise vortex behavior during oblique shock/vortex interaction," *Shock Waves*, Vol.8, pp.243-255.
- [4] 1985, Ribner, H.S., "Cylindrical sound wave generated

- by shock-vortex interaction," *AIAA Journal*, Vol.23, pp.1708-1705.
- [5] 1999, Inoue, O. and Hattori, Y., "Sound generation by shock-vortex interaction," *Journal of Fluid Mechanics*, Vol.380, pp.81-116.
- [6] 2000, Grasso, F. and Pirozzoli, S., "Shock wave - vortex interactions: shock and vortex deformations, and sound production," *Theoretical and Computational Fluid Dynamics*, Vol.13, pp.421-456.
- [7] 2005, Zhang, S.H., Zhang, Y.T. and Shu, C.W., "Multistage interaction of a shock wave and a strong vortex," *Physics of Fluids*, Vol.17, 116101.
- [8] 2014, Xiao, H. and Myong, R.S., "Computational simulations of microscale shock-vortex interaction using a mixed discontinuous Galerkin method," *Computers & Fluids*, Vol.105, pp.179-193.
- [9] 1949, Liebermann, L., "The second viscosity of liquids," *Physical Review*, Vol.76, p.440.
- [10] 1990, Emanuel, G., "Bulk viscosity of a dilute polyatomic gas," *Physics of Fluids A: Fluid Dynamics*, Vol.2, pp.2252-2254.
- [11] 1995, Gad-el-Hak, M., "Questions in fluid mechanics," *Journal of Fluid Engineering*, Vol.117, pp.3-5.
- [12] 1999, Graves, R.E. and Argrow, B.M., "Bulk viscosity: past to present," *Journal of Thermophysics and Heat Transfer*, Vol.13, pp.337-342.
- [13] 2004, Myong, R.S., "A generalized hydrodynamic computational model for rarefied and microscale diatomic gas flows," *Journal of Computational Physics*, Vol.195, pp.655-676.
- [14] 1981, Curtiss, C.F., "The classical Boltzmann equation of a gas of diatomic molecules," *Journal of Chemical Physics*, Vol.75, pp.376-378.
- [15] 2001, Eu, B.C. and Ohr, Y.G., "Bulk viscosity, and sound wave absorption and dispersion in dilute rigid molecular gases," *Physics of Fluids*, Vol.3, pp.744-753.
- [16] 1997, Bassi, F. and Rebay, S., "A high-order accurate discontinuous finite element method for the numerical solution of the compressible Navier-Stokes equations," *Journal of Computational Physics*, Vol.131, pp.267-279.
- [17] 2014, Le, N.T.P, Xiao, H. and Myong, R.S., "A triangular discontinuous Galerkin method for non-Newtonian implicit constitutive models of rarefied and microscale gases," *Journal of Computational Physics*, Vol.273, pp.160-184.
- [18] 1998, Cockburn, B. and Shu, C.W., "The Runge-Kutta discontinuous Galerkin method for conservation laws V: multidimensional systems," *Journal of Computational Physics*, Vol.141, pp.199-224.